

(Fig. 3A). Pt deposition resulted in three distinct levels of contrast that reflect the surface height, with the lowest level being the original Au terraces (Fig. 3B). The same three-level structure was observed independently of deposition time up to 500 s (Fig. 3C). The middle contrast level corresponds to a high density of Pt islands that covered ~85% of the Au surface, with a step height of ~0.24 nm, consistent with XPS results. Inspection with a higher rendering contrast revealed a ~10% coverage of a second layer of small Pt islands with a step height ranging between 0.23 and 0.26 nm (Fig. 3D). Step positions associated with the flame-annealed substrate were preserved, with negligible expansion or overgrowth of the 2D Pt islands occurring beyond the original step edge. The lateral span of the Pt islands was 2.02 ± 0.38 nm, corresponding to an area of 4.23 ± 1.97 nm². Incipient coalescence of the islands was constrained by surrounding (dark) narrow channels, 2.1 ± 0.25 nm wide, that account for the remaining Pt-free portion of the first layer. The reentrant channels correspond to open Au terrace sites that were surrounded by adjacent Pt islands in what amounted to a huge increase in step density relative to the original substrate, the net geometric or electronic effect of which was to block further Pt deposition. The chemical nature of the inter-island region was assayed by exploiting the distinctive voltammetry of Pt and Au with respect to H_{upd} and oxide formation and reduction (fig. S2 and supplementary text).

Similar three-level Pt overlayers have been observed for monolayer films produced by molecular beam epitaxy (MBE) deposition at 0.05 monolayers/min (20). Pt-Au intermixing driven by the decrease in surface energy that accompanies Au surface segregation was evident. In the present work, Pt monolayer formation was effectively complete within 1 s, giving a growth rate three orders of magnitude greater than in the MBE-STM study. Exchange of the deposited Pt with the underlying Au substrate was expected to be less developed. However, intermixing and possible chemical contrast (i.e., the ligand effect) were evident on limited sections of the surface that were correlated with the original faulted geometry of the partially reconstructed Au surface. Upon lifting of the reconstruction, the excess Au atoms expelled mark the original fault location as linear 1D surface defects in the Pt overlayer (Fig. 3E). A simplified schematic of the self-terminating Pt deposition process in Fig. 3F describes how the H_{upd} accompanying incremental expansion of the 2D Pt islands can hinder the development of a second Pt layer, presumably by perturbation of the overlying water structure (17). This rapid process resulted in a much higher Pt island coverage than has been obtained by other methods, such as galvanic exchange reactions.

Because the saturated H_{upd} coverage is the agent of termination, reactivation for further Pt deposition was possible by removing the upd layer by sweeping or stepping the potential to positive values, e.g., $>+0.2 V_{\text{SSCE}}$ where negligible Pt dep-

osition occurs. Sequential pulsing between $+0.4 V_{\text{SSCE}}$ and $-0.8 V_{\text{SSCE}}$ enabled Pt monolayer deposition to be controlled in a digital manner. EQCM was used to track the mass gain, showing two net increments per cycle (Fig. 4A). We attributed the mass gain to a combination of Pt deposition [486 ng/cm^2 for a monolayer of Pt(111)], anion adsorption and desorption (41 ng/cm^2 for $7 \times 10^{14} \text{ Cl}^-$ ion/cm², 117 ng/cm^2 for a 0.14 fractional coverage of PtCl_4^{2-}) (7, 21), and coupling to other double-layer components such as water. The anionic mass increments were expected to be asymmetric for the first cycle on the Au surface, but once it was covered, subsequent cycles only involved Pt surface chemistry. After correcting for the electroactive surface area of the Au electrode ($A_{\text{real}}/A_{\text{geometric}} = 1.2$, derived from reductive desorption of Au oxide in perchloric acid), the net mass gain for each cycle indicates that a near-pseudomorphic layer of Pt was deposited. XPS analysis of Pt films grown in various deposition cycles gave remarkably good agreement with EQCM data (Fig. 4B). The ability to rapidly manipulate potential and double-layer structure, as opposed to the exchange of reactants, offers simplicity, substantially improved process efficiency, and far greater process speed than other surface-limited deposition methods.

References and Notes

1. F. T. Wagner, R. Lakshmanan, M. F. Mathias, *J. Phys. Chem. Lett.* **1**, 2204 (2010).
2. M. K. Debe, *Nature* **486**, 43 (2012).
3. M. T. M. Koper, Ed., *Fuel Cell Catalysis, A Surface Science Approach* (Wiley, Hoboken, NJ, 2009).
4. V. R. Stamenkovic et al., *Nat. Mater.* **6**, 241 (2007).
5. R. R. Adzic et al., *Top. Catal.* **46**, 249 (2007).
6. T. Michely, J. Krug, *Islands, Mounds and Atoms, Patterns and Processes in Crystal Growth Far from Equilibrium* (Springer Series in Surface Science, V42, Springer, New York, 2003).

7. H. F. Waibel, M. Kleinert, L. A. Kibler, D. M. Kolb, *Electrochim. Acta* **47**, 1461 (2002).
8. T. Kondo et al., *Electrochim. Acta* **55**, 8302 (2010).
9. I. Bakos, S. Szabo, T. Pajkossy, *J. Solid State Electrochem.* **15**, 2453 (2011).
10. S. R. Brankovic, J. X. Wang, R. R. Adzic, *Surf. Sci.* **474**, L173 (2001).
11. D. Gokcen, S.-E. Bae, S. R. Brankovic, *Electrochim. Acta* **56**, 5545 (2011).
12. B. W. Gregory, J. L. Stickney, *J. Electroanal. Chem.* **300**, 543 (1991).
13. A. J. Gregory, W. Levason, R. E. Noflre, R. Le Penven, D. Pletcher, *J. Electroanal. Chem.* **399**, 105 (1995).
14. See supplementary materials on Science Online.
15. N. Garcia-Araez, V. Climent, E. Herrero, J. Feliu, J. Lipkowski, *J. Electroanal. Chem.* **582**, 76 (2005).
16. D. Strmcnik, D. Tripkovic, D. van der Vliet, V. Stamenkovic, N. M. Markovic, *Electrochem. Commun.* **10**, 1602 (2008).
17. T. Roman, A. Groß, Structure of water layers on hydrogen-covered Pt electrodes. *Cataly. Today*; <http://dx.doi.org/10.1016/j.cattod.2012.06.001> (2012).
18. G. Jerkiewicz, G. Vatankhah, S. Tanaka, J. Lessard, *Langmuir* **27**, 4220 (2011).
19. P. J. Cumpson, M. P. Seah, *Surf. Interface Anal.* **25**, 430 (1997).
20. M. O. Pedersen et al., *Surf. Sci.* **426**, 395 (1999).
21. Y. Nagahara et al., *J. Phys. Chem. B* **108**, 3224 (2004).

Acknowledgments: We thank J. J. Mallett for his early observations on the difficulty of electrodepositing Pt films at negative potentials. This work was supported by NIST–Material Measurement Laboratory programs. The x-ray photoelectron spectrometer was provided by NIST–American Recovery and Reinvestment Act funds. Y.L. thanks the NIST–National Research Council Postdoctoral Fellowship Program for support. NIST has filed a provisional patent application (Atomic Layer Deposition of Pt from Aqueous Solutions) based on this work.

Supplementary Materials

www.sciencemag.org/cgi/content/full/338/6112/1327/DC1
Materials and Methods
Supplementary Text
Figs. S1 and S2
References (22–26)

16 August 2012; accepted 17 October 2012
10.1126/science.1228925

Phase Transformations and Metallization of Magnesium Oxide at High Pressure and Temperature

R. Stewart McWilliams,^{1,2*}† Dylan K. Spaulding,³‡ Jon H. Eggert,⁴ Peter M. Celliers,⁴ Damien G. Hicks,⁴ Raymond F. Smith,⁴ Gilbert W. Collins,⁴ Raymond Jeanloz^{3,5}

Magnesium oxide (MgO) is representative of the rocky materials comprising the mantles of terrestrial planets, such that its properties at high temperatures and pressures reflect the nature of planetary interiors. Shock-compression experiments on MgO to pressures of 1.4 terapascals (TPa) reveal a sequence of two phase transformations: from B1 (sodium chloride) to B2 (cesium chloride) crystal structures above 0.36 TPa, and from electrically insulating solid to metallic liquid above 0.60 TPa. The transitions exhibit large latent heats that are likely to affect the structure and evolution of super-Earths. Together with data on other oxide liquids, we conclude that magmas deep inside terrestrial planets can be electrically conductive, enabling magnetic field-producing dynamo action within oxide-rich regions and blurring the distinction between planetary mantles and cores.

Magnesium oxide (MgO) is among the simplest oxides constituting the rocky mantles of terrestrial planets such as

Earth and the cores of Jupiter and other giant planets. Present in Earth's mantle as an end-member component of the mineral (Mg,Fe)O magnesiowüstite,

it can be abundant in larger planets due to the theoretically expected dissociation of (Mg,Fe) SiO₃ perovskite (1). Among common planetary constituents, MgO is thought to be especially resistant to transformation under pressure and temperature, having a high melting temperature (2–7), a wide electronic band gap under pressure (1, 8, 9), and a simple phase diagram featuring three phases at the high pressures explored in the present study: the B1 (NaCl)-structured solid found at ambient conditions, the liquid state, and an as-yet-unobserved high-pressure crystalline phase having the B2 (CsCl) structure (1–5, 9, 10).

¹Geophysical Laboratory, Carnegie Institution of Washington, 5251 Broad Branch Road, NW, Washington, DC 20015, USA. ²Howard University, 2400 Sixth Street, NW, Washington, DC 20059, USA. ³Department of Earth and Planetary Science, University of California, Berkeley, CA 94707, USA. ⁴Physics Division, Physical and Life Science Directorate, Lawrence Livermore National Laboratory, Livermore, CA 94550, USA. ⁵Department of Astronomy and Miller Institute for Basic Research in Science, University of California, Berkeley, CA 94720, USA.

*To whom correspondence should be addressed. E-mail: stewartmwilliams@gmail.com

†Present address: Grupo de Geociencias, Departamento de Física, Universidad de Los Andes, Bogotá, Colombia

‡Present address: Commissariat à l’Énergie Atomique, Département de Physique Théorique et Appliquée, Bruyères le Châtel, 91297 Arpajon Cedex, France.

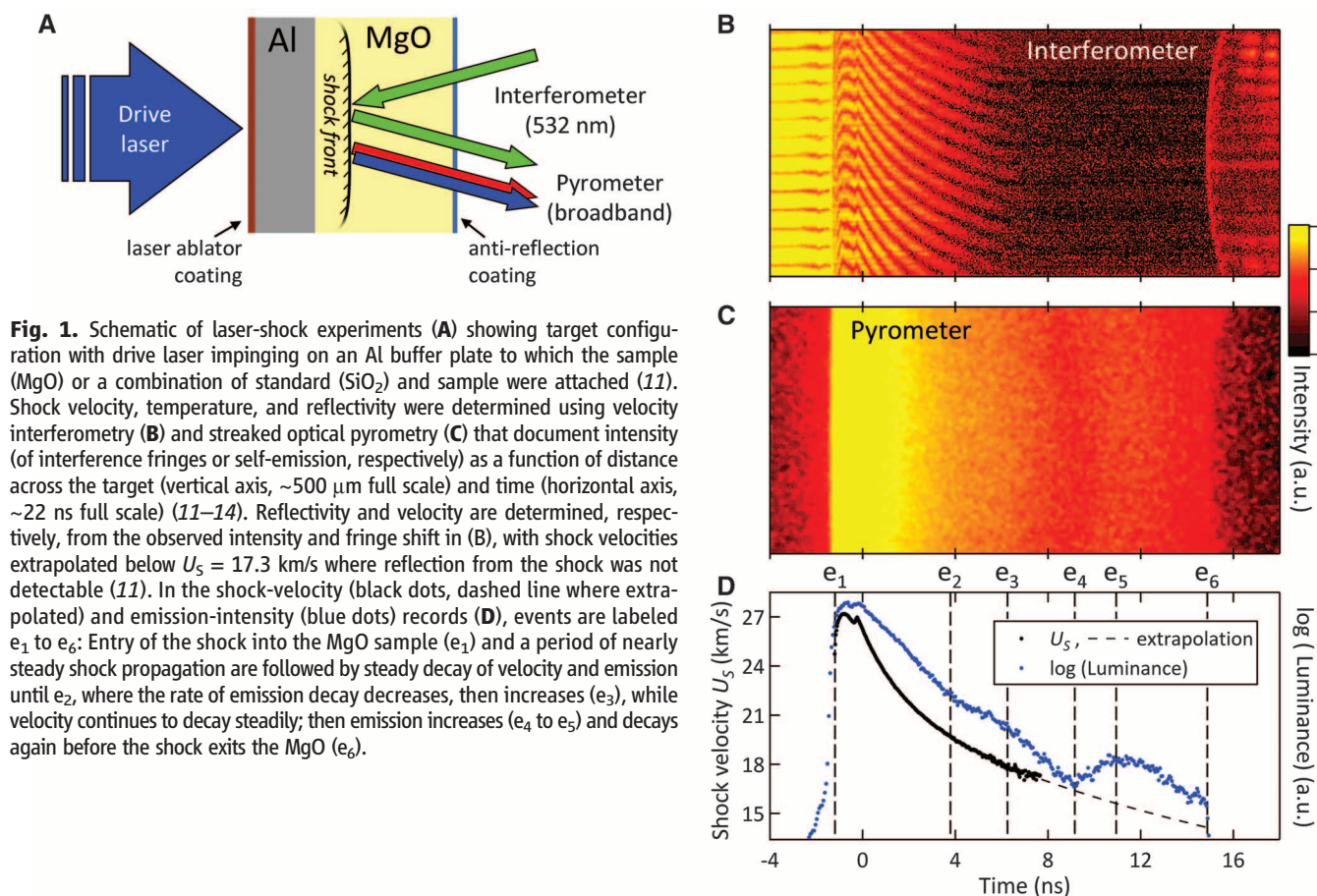
To characterize MgO at the elevated pressures and temperatures of planetary interiors, we measured its pressure-volume (P , V) equation of state to 0.6 TPa (6 Mbar) and its temperature (T) and optical reflectivity (R) to beyond 1.4 TPa (14 Mbar) and 50,000 K under shock loading (11). We determined shock temperature and corresponding shock velocity (U_S) using the method of decaying shocks (11–14), in which an optically thick and reflecting shock wave decreases in amplitude as it propagates, revealing—through time-resolved measurement of emission, velocity, and reflectivity—the properties of a continuum of shock states (Fig. 1). Determining the corresponding particle velocity (U_P) in separate experiments (Fig. 2 and fig. S1) allows for the derivation of pressure and volume from our measurements (11, 15).

We observe that the shock temperature does not change monotonically with pressure, as expected for a single phase (15, 16), but instead shows a large anomaly with a temperature minimum at about 0.45 TPa and 8500 K (Figs. 1 and 2). Two additional regions of anomalous behavior (at about 0.65 TPa and beyond 1 TPa) are most evident when examining the specific heat, C_V , of the shock states (Fig. 2B) (11–13). In broad regions of our data, C_V closely matches the Dulong-Petit limit ($C_V = 6 R_{\text{gas}}$, where R_{gas} is the gas constant per mole of atoms), consistent

with the presence of a pure MgO phase above the Debye temperature (~ 760 K) (12, 13, 15); in three distinct regions, however, there is substantial deviation from this value. The anomalous values of C_V suggest the influence of latent heats associated with structural, bonding or electronic transitions.

Indeed, beginning with the second transition (0.55 TPa) there is an increase in optical reflectivity (Fig. 2C) from $\sim 0.5\%$ —a value consistent with the optical properties of low-pressure, insulating MgO (17) (figs. S2 and S3)—toward $\sim 20\%$, indicating substantial changes in electronic properties. A simple (Drude-semiconductor) model of the measured reflectivities (11–13) is consistent with the energy gap between valence and conduction electronic bands nearly vanishing during the second transition (Fig. 2C), resulting in metallic conductivities $>10^4$ S/m above 0.60 to 0.70 TPa (fig. S4) (11).

To interpret these experimental results, we constructed a Mie-Grüneisen-Debye, finite-strain equation-of-state (16, 18) for MgO constrained by the shock data (11). From this model, we assess phase-transition properties, such as the volume and entropy of transformation (ΔV_{tr} and ΔS_{tr} , respectively). We find that the low-pressure behavior of MgO (to 0.35 TPa and 9500 K) is well described with this model, taking parameters solely from measurements on B1-MgO near



ambient conditions (e.g., pressures below 0.005 TPa) (19). Beyond 0.35 TPa, a sequence of phase transformations is required to explain the anomalies in shock temperature, consistent with our specific heat analysis (Table 1).

Several interpretations are possible for the first, most prominent transition, although the observed decrease in shock temperature indicates a positive entropy change (positive latent heat) from low- to high-pressure phases. If the transformation occurs at thermodynamic equilibrium, the data follow a phase boundary having a negative Clapeyron slope and implying a volume change as negative as $\Delta V_{tr}/V \sim -7\%$ (Table 1) (11, 15). This suggests that the first transition corresponds with solid-solid transformation and the second [consistent with positive volume and entropy change (Table 1)] with melting. Indeed, pressure-temperature conditions of the first and second transitions, and Clapeyron slopes obtained assuming equilibrium transformation, are close to theoretically predicted values for the B1-B2 and melting transitions of MgO (Table 1) (2). Alternatively, the first transition could be due to melting (3), with associated superheating upon shock compression (12). In this case, the first transformation can have negligible volume change (Table 1) (11), and the second corresponds with a transformation in the fluid.

Our preferred interpretation is that the two transitions are due to B1-B2 (0.45 TPa) and B2-melt (0.65 TPa), respectively. The second transformation is unlikely to be anything other than melting; there is no theoretical evidence for a liquid-liquid transition in MgO (8), and known fluid-fluid transitions in other shock-compressed insulators typically occur over a much broader pressure and temperature range (12, 13). Also, the transition from electrically insulating solid to metallic liquid in this interpretation is consistent with theoretical predictions of electronic properties for MgO (1, 8, 9) (fig. S4) and reflects the melting behavior of other nonmetals such as carbon (13), silicon, and sulfur (20).

Continuous changes in the reflectivity of the liquid state suggest that liquid electronic properties are strongly sensitive to temperature and pressure (8). The large entropy of the first transition relative to typical solid-solid transitions remains poorly understood but is consistent with available theory for MgO (Table 1). The broad region of anomalously high specific heat beyond ~ 1 TPa and $\sim 33,000$ K is similar to that observed at extreme temperatures in carbon and SiO₂ (12, 13) and is similarly attributed here to the onset of complex fluid bonding or to increased electronic specific heat. With this interpretation, we have a self-consistent picture for the phase diagram of MgO (Fig. 3), involving two crystalline phases (B1 and B2) and one liquid phase (1–4, 9, 10).

We conclude that MgO is solid at conditions found in the present Earth (21), in large Earth-like

Fig. 2. Shock temperature *T* (A), specific heat *C_v* (B), and shock-front reflectivity *R* (C) measured for MgO in two experiments [blue and red solid curves, systematic uncertainty bounds (11) shown by dotted curves (mean \pm SD)] are shown as a function of shock-wave velocity (bottom scale) and pressure (top scale), determined from a linear *U_s-U_p* equation-of-state (D) based on a fit (11) to data at low pressure (30–33) (off scale, fig. S1) and high pressure (open symbols, table S1) measured (34) relative to SiO₂ (35). A Drude-semiconductor model fit to the reflectivity data is shown by the green curve in (C) (11); solid and dashed black lines indicate the band gap (*E_g*) for models constrained to the zero-pressure value for MgO, or not, respectively. Events, labeled as in Fig. 1, correspond to transitions between anomalous (gray shading) and normal (*R_{gas}*) values of *C_v*.

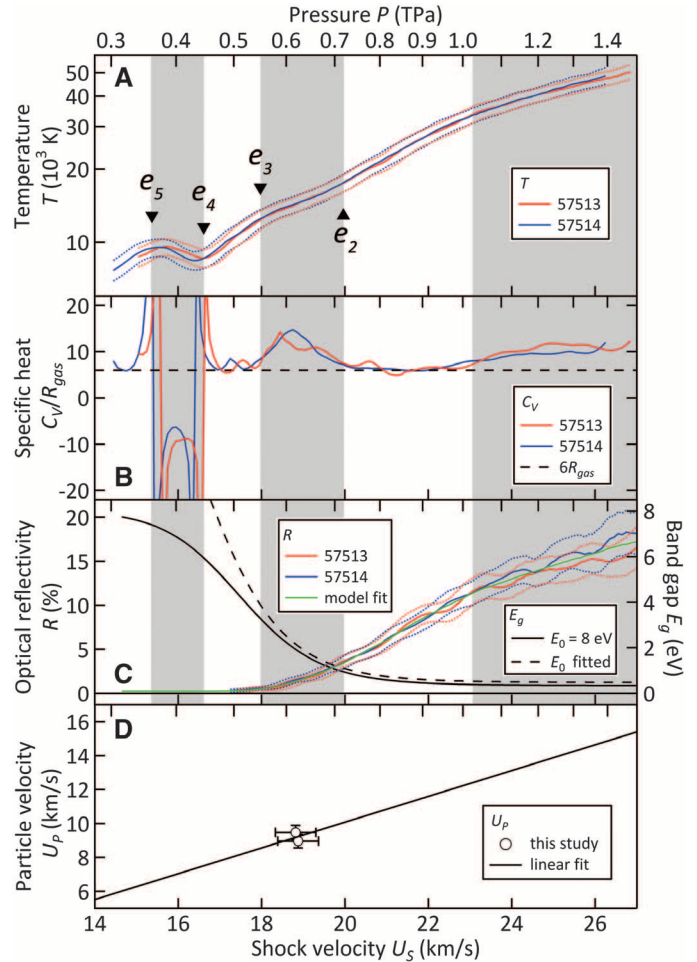


Table 1. Comparison between experimental and theoretical properties of phase transitions in MgO. Experimental ranges include thermodynamic equilibrium and nonequilibrium [e.g., superheating (12)] interpretations of the transitions (11). The Clapeyron slope is $(\partial P/\partial T)_B$. Uncertainties are mean \pm SD.

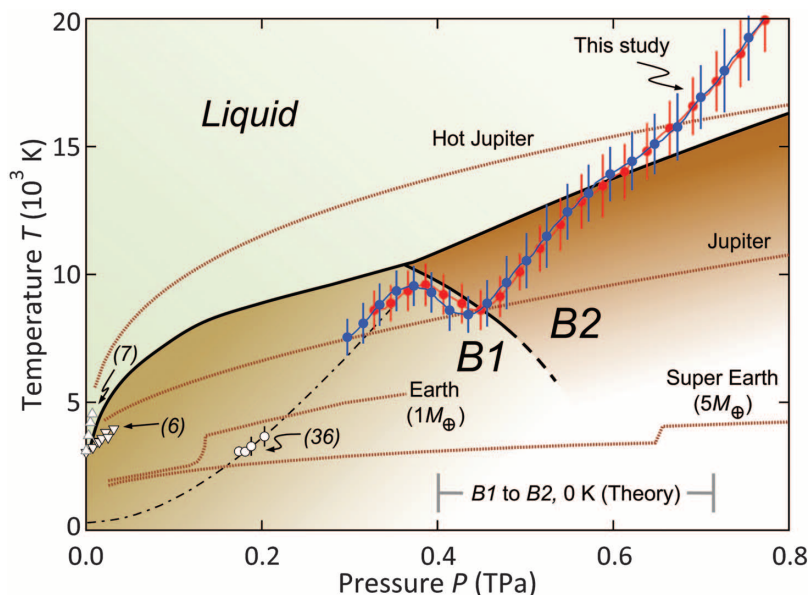
		<i>P</i> (TPa)	<i>T</i> (10 ³ K)	$(\partial P/\partial T)_B$ (10 ⁻⁴ TPa/K)	$\Delta S_{tr} / R_{gas}$	$\Delta V_{tr} / V$ (%)
1st transition	Experiment (this study)	0.44 \pm 0.08	9.0 \pm 0.7	-3.9 \pm 3.0	3.9 \pm 0.6	-3.8 \pm 3.1
	B1-B2 (theory)	0.33 \pm 0.04 (2)	8.1 \pm 0.7 (2)	-0.60 \pm 0.18 (2)	1.9 \pm 0.9†	-4.0 \pm 0.8† (9)
2nd transition	Experiment (this study)	0.65 \pm 0.05	14.0 \pm 1.1	1.2 \pm 0.8	1.6 \pm 0.1	4.1 \pm 2.9
	Melt (theory)	0.59 \pm 0.05 (2)	13.6 \pm 0.6 (2)	0.77 (2)	0.5 \pm 0.1‡	0.9 \pm 0.2‡ (3, 8)

†Upper bound, assuming $\Delta V_{tr}/V$ to be constant along the phase boundary, and calculating ΔS_{tr} from the Clausius-Clapeyron relation $(\partial P/\partial T)_B = \Delta S_{tr}/\Delta V_{tr}$; lower bounds are $\Delta S_{tr} \sim 0$ and $\Delta V_{tr} \sim 0$, obtained if ΔS_{tr} is presumed to be constant along the boundary above zero temperature and infinitesimal (11). ‡Estimated assuming that $\Delta V_{tr}/V$ on the melting curve is similar at high pressure for the B1 and B2 phases and using the Clapeyron relation to calculate ΔS_{tr} .

planets (22) and—based on extrapolations of the melting curve—in Jupiter and its core (23) (Fig. 3). The B2 phase of MgO is likely to be stable in the deep mantles of Earth-like planets of more than four Earth masses (22) (Fig. 3), so a B1-B2 transition can be relevant to planetary iron-bearing magnesiowüstite (24). With the corresponding decrease in volume (up to 7%) and

large latent heat of transformation (Table 1), a B1-B2 transition could influence internal structure and dynamics (22, 25), orbital evolution (25), and exoplanet mass-radius relationships (22). This is particularly true for terrestrial planets exceeding ~ 8 Earth masses (22), where dissociation of perovskite (1) could make magnesiowüstite the most abundant mineral of the deep mantle.

Fig. 3. Phase diagram of MgO constructed from shock temperature data [solid circles, this study, red and blue for two shots; open black circles (36)] with B1-phase temperature model (dot-dashed black line) (36). Our proposed phase diagram (heavy black lines) is a modification of the recent theoretical phase diagram of (2, 4), in which the melt curve is roughly identical but the B1-B2 transition has moved to higher pressure. Zero-temperature B1-B2 transition pressures from theory (excluding outliers) are given by the gray bracket (10). Experimental melting temperatures (6, 7) are open triangles. Also shown are the conditions of planetary interiors for Earth (21), a theoretical Earth-like planet of 5 earth masses (Super Earth) (22), Jupiter (23), and a hot Jupiter-mass planet (average prediction) (37); temperature discontinuities at 0.13 and 0.65 TPa in the terrestrial planets correspond to the base of the oxide mantle.



Major end-member oxides of deep planetary interiors (1)—SiO₂ (12), MgSiO₃ (14), and MgO—uniformly exhibit high electrical conductivities (σ) in their fluid states at high pressure and temperature, consistent with metallic or semi-metallic behavior: $\sigma \sim 10^3$ to 10^5 S/m at $T \sim 5000$ to 15,000 K and $P \sim 0.1$ to 0.7 TPa. Planetary magmas composed of these rocky constituents should likewise be highly conductive at high pressure, as compared with magmas familiar at Earth's surface ($\sigma \sim 10^{-2}$ to 10^2 S/m) (26), and would thereby resemble liquid iron alloys making up planetary cores (27).

Our experiments therefore reveal a blurring between traditional definitions of planetary mantle and core material: Liquid oxides can be considered either molten mantle constituents or electrically conducting core components. Indeed, for terrestrial planets with extensive melting (i.e., magma oceans) and sufficient interior pressure, oxides could contribute to the dynamo process sustaining a planetary magnetic field. The magnetic Reynolds number $R_m = \mu_0 \sigma v L$ (28) for such a magma ocean ($R_m \sim 10^3$ to 10^7) exceeds the critical value required for a self-sustaining field ($R_m > 10^1$ to 10^2), considering flow velocities v appropriate for a terrestrial magma ocean (4 to 40 m/s) (29), and distance scales L appropriate for terrestrial mantles (10^6 to 10^7 m); μ_0 is the permeability of free space. Although Earth may be too small ($P < 0.13$ TPa in the mantle) for substantially elevated oxide conductivity, even a modest (order of magnitude) increase in σ over typical magma values can shift R_m in an early-Earth magma ocean from too small ($R_m \sim 10^{-2}$ to 10^2) to large enough to sustain dynamo action. This suggests that an early, short-lived magnetic field could have existed on Earth, perhaps similar to those inferred for Mars and the Moon on the basis of remnant crustal magnetism.

References and Notes

1. K. Umemoto, R. M. Wentzcovitch, P. B. Allen, *Science* **311**, 983 (2006).
2. A. B. Belonoshko, S. Arapan, R. Martonak, A. Rosengren, *Phys. Rev. B* **81**, 054110 (2010).
3. N. de Koker, L. Stixrude, *Geophys. J. Int.* **178**, 162 (2009).
4. D. Alfé, *Phys. Rev. Lett.* **94**, 235701 (2005).
5. A. Aguado, P. A. Madden, *Phys. Rev. Lett.* **94**, 068501 (2005).
6. A. Zerr, R. Boehler, *Nature* **371**, 506 (1994).
7. L. Zhang, Y. W. Fei, *Geophys. Res. Lett.* **35**, L13302 (2008).
8. B. Karki, D. Bhattarai, L. Stixrude, *Phys. Rev. B* **73**, 174208 (2006).
9. A. R. Oganov, M. J. Gillan, G. D. Price, *J. Chem. Phys.* **118**, 10174 (2003).
10. D. Alfé *et al.*, *Phys. Rev. B* **72**, 7 (2005).
11. Materials and methods are available as supplementary materials on Science Online.
12. D. G. Hicks *et al.*, *Phys. Rev. Lett.* **97**, 025502 (2006).
13. J. H. Eggert *et al.*, *Nat. Phys.* **6**, 40 (2010).
14. D. K. Spaulding *et al.*, *Phys. Rev. Lett.* **108**, 065701 (2012).
15. Y. B. Zel'dovich, Y. P. Raizer, in *Physics of Shock Waves and High-Temperature Hydrodynamic Phenomena*. W. D. Hayes, R. F. Probstein, Series Eds. (Dover Publications, Inc., Mineola, New York, 2002).
16. R. G. McQueen, S. P. Marsh, J. W. Taylor, J. N. Fritz, W. J. Carter, in *High-Velocity Impact Phenomena*, R. Kinslow, Ed. (Academic Press, New York, 1970), pp. 293–417.
17. G. D. Stevens, L. R. Veerer, P. A. Rigg, R. S. Hixson, *AIP Conf. Proc.* **845**, 1353 (2006).
18. R. Jeanloz, *J. Geophys. Res.* **94**, (B5), 5873 (1989).
19. T. J. Ahrens, Ed., *AGU Handbook of Physical Constants*, vol. II (1995), pp. 45–97.
20. D. A. Young, *Phase Diagrams of the Elements* (Univ. of California Press, Berkeley, 1991).
21. S. Tateno, K. Hirose, Y. Ohishi, Y. Tatsumi, *Science* **330**, 359 (2010).
22. D. Valencia, R. J. O'Connell, D. Sasselov, *Icarus* **181**, 545 (2006).
23. T. Guillot, *Annu. Rev. Earth Planet. Sci.* **33**, 493 (2005).
24. B. J. Wood, *Earth Planet. Sci. Lett.* **174**, 341 (2000).
25. S.-i. Karato, *Icarus* **212**, 14 (2011).
26. F. Gaillard, G. I. Marziano, *J. Geophys. Res. Solid Earth* **110**, 12 (2005).
27. E. Knittle, R. Jeanloz, *Geophys. Res. Lett.* **13**, 1541 (1986).
28. D. J. Stevenson, *Space Sci. Rev.* **152**, 651 (2010).
29. V. Solomatov, in *Origin of the Earth and Moon*, R. M. Canup, K. Righter, Eds. (Univ. of Arizona Press, Tucson, 2000), pp. 323–338.
30. S. P. Marsh, *LASL Shock Hugoniot Data* (Univ. of California Press, Berkeley, 1980).
31. M. S. Vassiliou, T. J. Ahrens, *Geophys. Res. Lett.* **8**, 729 (1981).
32. T. S. Duffy, T. J. Ahrens, *J. Geophys. Res. Solid Earth* **100**, (B1), 529 (1995).
33. L. Zhang, Z. Z. Gong, Y. W. Fei, *J. Phys. Chem. Solids* **69**, 2344 (2008).
34. D. G. Hicks *et al.*, *Phys. Rev. B* **78**, 174102 (2008).
35. M. D. Knudson, M. P. Desjarlais, *Phys. Rev. Lett.* **103**, 225501 (2009).
36. B. Svendsen, T. J. Ahrens, *Geophys. J. R. Astron. Soc.* **91**, 667 (1987).
37. I. Baraffe, G. Chabrier, T. Barman, *Astron. Astrophys.* **482**, 315 (2008).

Acknowledgments: We thank N. Gómez-Pérez, R. J. Hemley, D. C. Swift, R. E. Cohen, D. A. Dalton, and W. Unites for helpful discussions. This work was performed under the auspices of the U.S. Department of Energy by Lawrence Livermore National Laboratory in part under contract W-7405-Eng-48 and in part under contract DE-AC52-07NA27344. We also acknowledge financial support from the U.S. Army Research Office (grant 56122-CH-H), a Krell Institute Department of Energy (DOE) National Nuclear Security Administration (NNSA) graduate fellowship (contract DE-FC52-08NA28752), the DOE/NNSA National Laser User Facility Program, the Miller Institute for Basic Research in Science, and the University of California. Data are available in this manuscript and in the supplementary materials.

Supplementary Materials

www.sciencemag.org/cgi/content/full/science.1229450/DC1
Materials and Methods
Figs. S1 to S6
Tables S1 to S3
References (38–53)

29 August 2012; accepted 26 October 2012
Published online 22 November 2012;
10.1126/science.1229450